Signal, Image and Video Processing
https://doi.org/10.1007/s11760-018-1320-y

ORIGINAL PAPER

Fully automatic prostate segmentation in MR images using a new hybrid active contour-based approach

Ahad Salimi[1] · Mohammad Ali Pourmina[1] · Mohammad-Shahram Moin[2]

Received: 26 October 2017 / Revised: 13 May 2018 / Accepted: 11 June 2018

Abstract

Precise prostate segmentation in magnetic resonance (MR) images is mostly utilized for prostate volume estimation, which can help in the determination of prostate-specific antigen density. In this paper, a fully automatic method that contains three successful steps to segment the prostate area in MR images was presented. This method includes a preprocessing stage, an automatic initial point generation step and an active contour-based algorithm with an external force known as vector field convolution (VFC). First, both noise and roughness are approximately removed using Sticks filter and morphology smoothing method. Then, an initial point is automatically generated using multilayer perceptron neural network to initiate the segmentation algorithm. Finally, VFC is employed to extract the prostate region. This system was tested on image data sets to detect the prostate boundaries. Results show that the proposed method can reach a DSC value of 86 ± 6%, is faster than existing methods and also more robust as compared to other methods.

Keywords Neural network · Active contour · Prostate segmentation · Sticks filter · Morphology smoothing

1 Introduction

Prostate cancer is the third leading cause of cancer death among American men, after lung and colorectal cancers (26,730 of 161,360) [1,2]. Magnetic resonance (MR) and transrectal ultrasound (TRUS) are widely employed as powerful imaging methods in different treatment phases like application of "the tumor biopsy", estimating the prostate volume and determining disease development [3]. Currently, in most treatments and diagnosis techniques (that is, measurement of prostate volume), the prostate region in images is manually outlined by physicians. The prostate manual segmentation is an extremely time-consuming and tedious process, which certainly causes many human mistakes, especially when numerous images are to be studied. Therefore, scheming an automatic prostate segmentation method in the mentioned images would significantly improve the prostate identification process. However, variety of gray levels, low signal-to-noise ratio (SNR), likeliness to the nearby textures, weak edges and artifacts make segmentation difficult and challenging. Prostate segmentation can be generally categorized into four main categories: contour- and shape-based methods, region-based methods, supervised and unsupervised clustering-based methods and hybrid methods.

In the contour- and shape-based approaches, the objects of interest are simply extracted using boundary and edge information. These methods can be categorized into five subgroups: active contour (AC), level sets, active shape and appearance models (ASM and AAM), deformable meshes, and curve-based segmentation. AC models usually utilize an energy function minimization manner to segment the prostate region. It is worth mentioning that a specific version of the AC model that uses the prior created shape from the coarse segmentation [4] has also been introduced as an approach to detect the prostate edges. Other prostate edge determination techniques include the level sets repeated in a sliced rotational framework [5,6] and a level-set method combined with the shape information [7]. A minimum description length Group-Wise image registration method and a multistart optimization scheme are used to match the AAM model in the new images [8].

In the region-based schemes, the local statistical features including mean, standard deviation and covariance are gen-

✉ Mohammad Ali Pourmina
pourmina@srbiau.ac.ir

[1] Department of Electrical and Computer Engineering, Science and Research Branch, Islamic Azad University, Tehran, Iran

[2] Faculty of Information Technology, ICT Research Institute, Tehran, Iran

Journal: 11760 MS: 1320 ☐ TYPESET ☐ DISK ☐ LE ☐ CP Disp.:2018/6/16 Pages: 9 Layout: Large

erally used in an optimizing approach for the prostate area detection. In this category, variation in the achieved outcomes usually depends on the definition of the objective function and the optimization procedure performance. These methods are further grouped into atlas, graph-cut and level-set schemes. In the work of Mahapatra et al. [9], the semantic data obtained by random forest clustering were used by the graph-cut algorithm to generate an objective function. Tian et al. [10] minimized an energy function which was based on a graph cut to distinguish the prostate from the background image. The energy function has also been constructed using a super pixel-based shape data term, two super pixel-based smoothness terms, and an appearance data term. Other works have reported other algorithms such as a 3-D graph cut that optimizes an objective function [11], mappings transform manner that converts an image to the adjusted edge distance map [12], and a new atlas-based scheme [13].

In the clustering-based techniques, image features such as filter frequency response and intensity are typically utilized to classify images. Here, features are usually used as a vector in the segmentation, which leads to greater accuracy in the presence of image artifact and noise. Gaussian mixture model and trained supervise initializing plan have been also used to segment the CG area [14,15]. The statistical model is created using the PCA execution on the inner probability propagation of the prostate area and the resulting contours of the landmark points. Conventional neural networks (CNN) have been widely used to segment prostate in MR images over the past few years. Yu et al. [16] presented a volumetric CNN with mixed residual connections that improves the segmentation accuracy, using the forward propagation of the location information and the smooth backward propagation of the gradient flow. Other works have also utilized CNN with either a boundary model provided by an adaptive feature learning probability boosting tree [17] or a combined convolutional neural network optimization framework [18].

In the hybrid methods, some of the local features such as texture, shape and the resulting data by clusters are used for better performance against artifact and noise. For example, a combination of graph-cut and level-set framework in an iterative hybrid system has been used for the 3-D object estimation in MR images [19]. However, the level sets are more accurate than the other methods. Thereby, researchers have utilized a 3-D graph cut to initialize level-set framework. Martin et al. [20] applied a likely atlas for employing the spatial information in order to extract the 3-D model of prostate volume. In this article, combination of texture and shape information was used based on the method presented in [21]. In another work, fully convolutional networks (FCNs) were combined with fully convolutional residual networks (FC-ResNets) [22], which was followed by generation of segmentation prediction using the normalized images that are refined by means of the FC-ResNet.

In this paper, a fully automatic prostate segmentation system was proposed for MR images. The system contains several stages, including preprocessing, initial point generation using a multilayer perceptron (MLP) neural network and prostate segmentation based on a vector field convolution (VFC) algorithm [23]. Finite capture range, noise sensitivity and poor convergence to the concavities are typical problems of the active contour or snake approach which is widely used in medical image segmentation. In this work, the VFC was employed as a constraint force to minimize the disadvantages of snakes and enhance convergence speed. On the other hand, the external force field of VFC was computed by convolving a vector field kernel with an edge map, derived from the gray-level image. The remaining part of this paper is organized as follows: Sect. 2 describes the proposed method for prostate segmentation, Sect. 3 presents the detailed experiments and results obtained by applying the proposed system to a typical prostate MR image, Sect. 4 gives a brief discussion of the results, and Sect. 5 concludes the paper.

2 Proposed automatic prostate segmentation system

As shown in Fig. 1, the proposed method is a three-phase intelligent system. First, two consecutive processes were applied to the input image in the preprocessing stage, which includes applying a Sticks filter and morphology smoothing. Second, an initial point generation stage was used based on MLP neural networks, which was trained to extract several features from the MR images. It is used to automatically obtain an initial contour for the active contour algorithm. Third, among the various medical image segmentation methods, the prostate region was detected using the VFC active contour, which has a lower execution time and higher accuracy than other active contour-based methods, as shown in the results section.

2.1 Preprocessing

The MR images used in this study were highly corrupted by roughness, and the edges of objects were not sufficiently clear. Therefore, usual segmentation algorithms produced segmentation leakage. To reduce this problem, a preprocessing step including combination of the Sticks filter and the morphology smoothing was considered in the system. The Sticks filter [24] was used to successfully reduce the speckle and simultaneously enhance the edges and contrast of the MR images in the first step. In the second step, morphology smoothing was applied to reduce the image roughness made in the previous stage. A combination of top-hat and bottom-hat transformation was used for morphology smoothing as shown in Eq. (1):

Journal: 11760 MS: 1320 TYPESET DISK LE CP Disp.:2018/6/16 Pages: 9 Layout: Large

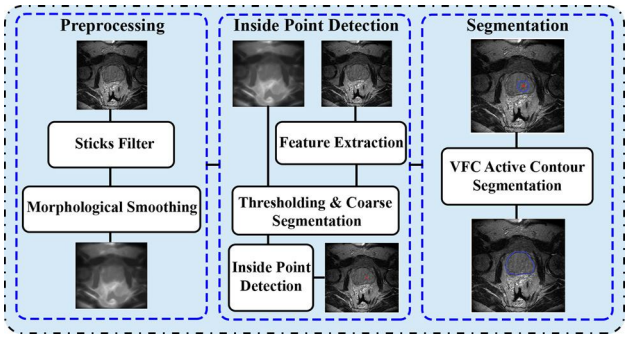

Fig. 1 Block diagram of the proposed system

$$I_S = I_{SF} + I_{TH} - I_{BH} \tag{1}$$

where I_S is the smoothed image, and I_{SF}, I_{TH} and I_{BH}, are the Sticks filtered output, the top-hat and bottom-hat transformation, respectively, that are given by Eq. (2):

$$\begin{aligned} I_{TH} &= I_{SF} - (I_{SF} \circ B_{mf}) \\ I_{BH} &= I_{SF} - (I_{SF} \bullet B_{mf}) \end{aligned} \tag{2}$$

where $\circ$ and $\bullet$ are the opening and closing operands, respectively, and B_{mf} is a disk with a 3-pixel radius.

2.2 Inside point detection

Active contour algorithm normally starts from an initial point (an inside point of the prostate area). In this work, two three-layer neural networks (NNs) [25] were used to generate the maximum (*MAXI*) and minimum (*MINI*) intensities of the prostate area. The initial point was created based on a proper method that uses the output of NNs as its thresholds. In order to train the NNs, a number of inputs and their corresponding targets are needed. The best values of the maximum and minimum intensities that lead to a rough segmentation of the prostate area are used as targets. As shown in Fig. 2, these intensities are extracted using the search within the prostate area, which is outlined by a physician in the training images. It means that the maximum and minimum intensities are found manually (using the trial and error method), which lead to the rough segmentation of the prostate area. On the other hand, for better performance of the training step, the NN inputs were selected as an averaging vector of the prostate area's intensities. A subregion of the image that is a rectangle region including the prostate area is needed to make the input vector. The subregion can be created using several mask images, which themselves are obtained by applying the thresholding to the manual outlined images. A mask image is a binary image, which is created based on the manual outlined result. (The inside and outside of the manual outlined area are selected as 1 and 0, respectively.) Then, the average of the mask images (a mask image is created for each of the

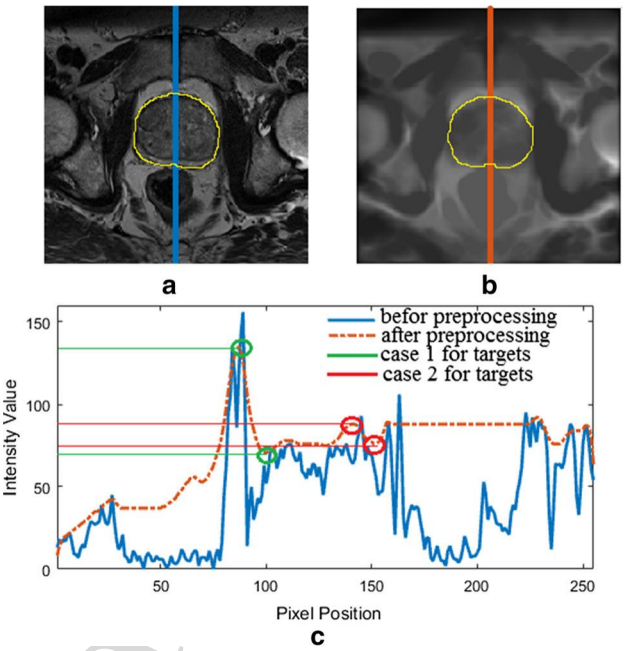

Fig. 2 Effects of the preprocessing stage on image. **a** The original image (yellow line: outlined prostate area by a physician), **b** image after preprocessing and **c** comparison of the intensity's profiles

training images) is calculated and converted to the binary image using the Otsu's method. The edge of the obtained object in the binary image was extracted, and its coordinates were determined ($X_b = [x_{ib}, y_{ib}]^T$). Finally, the subregion's coordinates (a rectangle with 4 fixed vertices) were obtained as follows:

$$\begin{aligned} &P_1 = [\min(x_{ib}), \min(y_{ib})],\ P_2 = [\max(x_{ib}), \min(y_{ib})] \\ &P_3 = [\max(x_{ib}), \min(y_{ib})],\ P_4 = [\max(x_{ib}), \max(y_{ib})] \end{aligned} \tag{3}$$

As shown in Fig. 3, the NN inputs are formed from the average values of the row profile of the subregion. These inputs are directly related to the statistical data of the prostate area. Then, the NNs were trained using the inputs and targets obtained of the training data set. Hence, a nonlinear polynomial is created between the statistical information and the targets. In the test phase, a similar input (like to the inputs created in the training phase) was made from each image to feed NNs. The NNs generated the suitable maximum and minimum intensities, and then, these values were used as thresholds to convert the input image to a binary class using Eq. (4):

$$B(x, y) = \begin{cases} 1 & MINI < I(x, y) < MAXI \\ 0 & \text{Otherwise} \end{cases} \tag{4}$$

where $B(x, y)$ and $I(x, y)$ are intensities in the binary and input images, respectively. As shown in Fig. 4, in the binary

Journal: 11760 MS: 1320 TYPESET DISK LE CP Disp.:2018/6/16 Pages: 9 Layout: Large

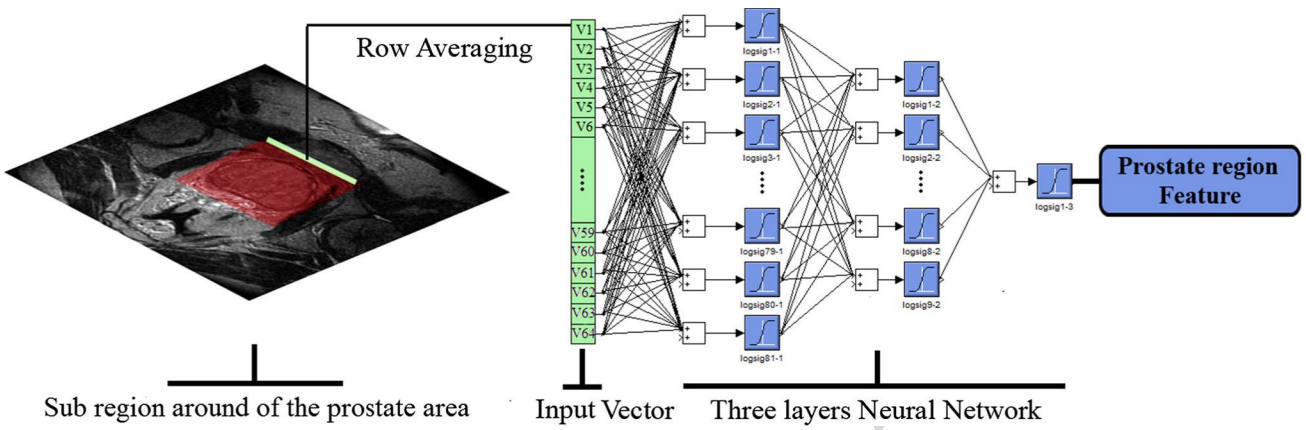

Fig. 3 The neural network structure. The inputs for the neural network in the training step (and test phase) are average values of the row profile of the subregion

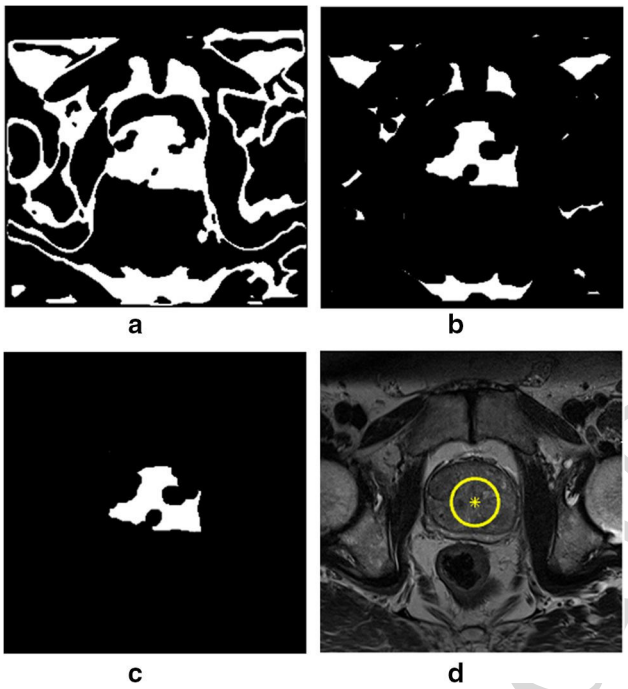

Fig. 4 The inside point generation stage. **a** The obtained binary image using the output features of the neural networks (rough segmentation), **b** the binary image after applying the erosion, **c** the object with the largest area and **d** the inside point and initial contour in the prostate region

class image, after applying an erosion step, the region with the largest area was selected as the rough segmentation of the prostate. Finally, the central pixel of the obtained region was considered as the initial point for the VFC algorithm.

2.3 VFC segmentation algorithm

In this step, the prostate boundaries are accurately extracted using an active contour-based framework, called vector flow convolution (VFC). The active contours or traditional snakes, which are attracted to the object boundaries, are generally represented by:

$$X(s) = [x_s, y_s], \; s \in [1, N] \tag{5}$$

where $[x_s, y_s]$ and N indicate the coordinates and the number of contour points, respectively. The active contour also deforms within the image, to minimize an energy function, which is defined as follows:

$$E_{AC} = \int_0^1 \left[\frac{1}{2} \left(\alpha \left| X'(s) \right|^2 + \beta \left| X''(s) \right|^2 \right) + E_{ext}(X(s)) \right] ds$$

$$E_{AC} = \int_0^1 \left[\frac{1}{2} E_{int}(X(s)) + E_{ext}(X(s)) \right] ds \tag{6}$$

where E_{int} and E_{ext} are the internal and external energies, respectively. The internal energy controls the snake's tension, rigidity and deformation, using α and β. The first and second derivatives of $X(s)$ with respect to s are indicated with $X'(s)$ and $X''(s)$, respectively. The external energy, E_{ext}, was also obtained from the image intensity. Some typical examples of external energy for the seeking edge are given by:

$$E_{ext}(x, y) = -|\nabla I(x, y)|^2$$
$$E_{ext}(x, y) = -|\nabla [G_\sigma(x, y) * I(x, y)]|^2 \tag{7}$$

where $I(x, y)$ and $G_\sigma(x, y)$ are the input image and the 2-D Gaussian function with standard deviation $sigma$, respectively. Linear convolution is denoted by *, and ∇ is the gradient operative. The external force, F_{ext}, was obtained from the external energy and defined to push the snake to the strong edges as follows:

$$F_{ext}(X) = -\nabla E_{ext}(X) \tag{8}$$

In this work, a proper external force called VFC was utilized to overcome the disadvantages of the traditional snake and GVF. The VFC is more robust to noise and initialization, has a lower computational cost, and is flexible to changes in the force field. To form an active contour that uses the VFC as its external force, a vector field kernel was defined as follows:

$$K(x, y) = m(x, y)n(x, y) \tag{9}$$

where $m(x, y) = (r + \varepsilon)^{-\gamma}$ is the vector magnitude at (x, y), γ is a positive parameter that determines the decreasing rate, ϵ is a very small positive constant, $n(x, y) = [\frac{-x}{r}, \frac{-y}{r}]$ ($n(0, 0) = [0, 0]$) indicates the unit vector to the origin, and $r = \sqrt{x^2 + y^2}$ is the distance of (x, y) from the origin. According to Eq. (9), the VFC external force $v(x, y) = [u(x, y), v(x, y)]$ is defined as follows:

$$v(x, y) = f(x, y) * K(x, y) \tag{10}$$

where $f(x, y)$ is the edge map of the input image, $k(x, y)$ is the vector field kernel and * represents the 2-D convolution operand. Since the value of $f(x, y)$ is larger around the main edges than the inside points of the object, the VFC external force pushes the free vector points to the main edges. This force is strongly correlated with $m(x, y)$, which is inspired by Newton's law of universal gravitation in physics [26]. The external energy is calculated using Eq. (8), and it can also be rewritten as follows:

$$\begin{aligned} &F_{\text{ext}} = -\nabla E_{\text{ext}} \ \rightarrow \ -div\, F_{\text{ext}} = \Delta E \\ &-\left(\frac{\partial u}{\partial x} + \frac{\partial v}{\partial y}\right) = \frac{\partial^2 E}{\partial^2 x} + \frac{\partial^2 E}{\partial^2 y} \ \rightarrow \ -K_c \\ &= \frac{\partial^2 E}{\partial^2 x} + \frac{\partial^2 E}{\partial^2 y} \end{aligned} \tag{11}$$

where Δ is the Laplacian operator and div is the divergence operator. Equation (11) is Poisson's equations with Dirichlet boundary conditions and its numerical solutions has been well studied [27]. In order to prevent the contour leakage in the searching process, an energy function for the contour shape constraint was introduced as follows:

$$E_{\text{shape}} = \frac{|\varphi_1|}{2} \sum_{i=1}^{N} \left|X_i - \bar{X} - \bar{R}e_i\right|^2 \tag{12}$$

where φ_1, $\bar{X}$, $\bar{R}$ and e_i are obtained from:

$$\begin{aligned} &\bar{X} = \tfrac{1}{N}\sum_{i=1}^{N} X_i, \quad \bar{R} = \tfrac{1}{N}\sum_{i=1}^{N} \left|\bar{X} - X_i\right| \\ &e_i = \left[\cos(\tfrac{2\pi i}{N}),\ \sin(\tfrac{2\pi i}{N})\right]^{\mathrm{T}}, \quad |\varphi_1| = |X_2 - X_1| \end{aligned} \tag{13}$$

Algorithm 1 : Optimizing process.

start
$X_i(0) \leftarrow X_i(t),\ T_{Stop} \leftarrow K_1,\ iteration \leftarrow K_2.$
$E_{old} \leftarrow \infty,\ t \leftarrow 0,\ er \leftarrow 0.$
while $t < iteration$ **do**
  $t \leftarrow t + 1$
  $E_{total} \leftarrow F_{obj}(X_i(t))$
  if $E_{old}(t) > E_{total}$ **then**
    $E_{old}(t) \leftarrow E_{total},\ X_{old} \leftarrow X_i(t-1).$
    else
    $er \leftarrow er + 1.$
  end if
  if $er > T_{Stop}$ **then**
    break.
  end if
  $X_i(t) \leftarrow X_i(t-1) + \Delta X_i.$
end while
end

According to the stated content, the objective function is defined as follows:

$$E_T(X_i) = E_{\text{int}} + \lambda E_{\text{shape}} + \kappa E_{\text{ext}} \tag{14}$$

where λ and κ are the impact parameters of the shape energy and the external energy, respectively.

2.4 The searching algorithm

In this section, how the objective function (Eq. 14) is optimized to lead to an accurate prostate segmentation, is discussed. The optimization process is an iterative algorithm that is stopped once certain conditions are met. First, an initial contour is placed in the prostate area using the features obtained by the neural networks. Then, the contour deforms under the influence of the internal energy and its deformation continues until the energy function is minimized. An error counter that counts the number of errors added once, going from step $t - 1$ to step t, is implemented here to prevent the contour from trapping into a local minimum during the optimization process. The user determines a threshold for the counting. The optimization process is stopped when the counter number becomes higher than the threshold or the iterative loop gets ended. This process is presented in Algorithm 1.

3 Experiments and results

To evaluate the proposed method, the prostate region was extracted from a series of T2-weighted MR images as provided by "Prostate MR Image Segmentation 2012 (PROMISE12)" challenge. The presented algorithm was executed in MATLAB, V-2015a. During the preprocessing phase, the Sticks filter with a mask length of 5 ($N = 5$) was used 3 times. Figure 2 shows the effect of two successive preprocessing stages on a typical MR image. As shown in Fig. 2c,

Journal: 11760 MS: 1320 TYPESET DISK LE CP Disp.:2018/6/16 Pages: 9 Layout: Large

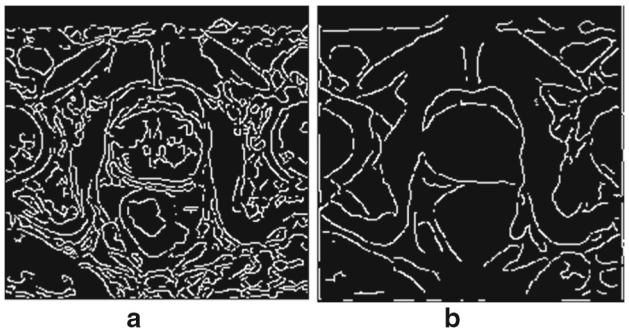

Fig. 5 The effects of preprocessing stage on the edge map. **a** The edge map of original image and **b** the edge map after preprocessing stage

the contrast around the edges was enhanced and the speckle was approximately removed. The preprocessing effect on the object edges, which was obtained using the Canny edge detector, is shown in Fig. 5. As mentioned in Sect. 2.2, the features of the prostate region were extracted using a pair of NN with three layers. The dimension of the obtained subregion (a rectangle) is 64 × 76 pixels. Then, the average pixel values of the row profile were used as the input for the NNs. Therefore, 64, 8 and 1 neurons were experimentally used in the first, second and third layers of the NNs, respectively. The logsig function was utilized in the first and second layers, and a linear function was used in the third layer. According to a learning rate of $L_{\text{rate}} = 0.001$, the NNs were trained with 550,000 iterations. Although the selected learning rate increased the NNs training time, the weights obtained after the training stage enhanced the algorithm accuracy, while the training set was randomly used to train the neural networks. Figure 6 shows the compression between the features for 25 randomly selected test images, which were obtained using trained neural networks and that determined manually. Figure 4 shows the rough segmented prostate region, performed by the initial point generation stage for a typical MR image. The initial contour was plotted according to the central pixel in the rough segmented prostate and the VFC active contour automatically outlined the prostate region. Figure 7 demonstrates the results of the prostate region segmentation at several random iterations using the introduced algorithm. The values of K_1 and K_2 were selected as 5 and 25 based on the tests done, and α, β, λ and κ were experimentally fixed to 0.2, 0.1, 100 and 200, respectively. The same method was applied for different slices of each MR image and appropriate results were obtained, as shown in Fig. 8. The shadow, artifacts and tissue similarity reduced the segmentation accuracy. As shown in Fig. 8, it especially occurred in the Apex slices.

4 Discussion

Accuracy of the proposed algorithm was also compared with the methods presented in "Prostate MR Image Segmentation" challenge. The metrics used in this study are the Dice similarity coefficient (DSC), relative absolute volume difference (RVD), the Hausdorff distance (HD) and the average boundary distance (ABD). DSC is defined as follows:

$$\text{DSC} = 2 \times \left[{}^{(A \cap B)}/_{(A \cup B)} \right] \quad (15)$$

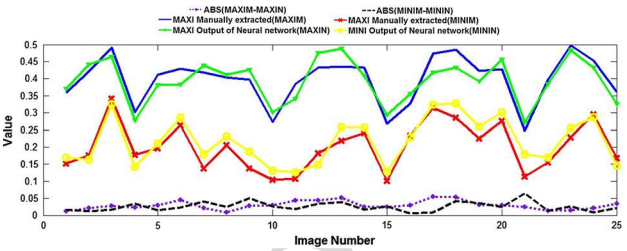

Fig. 6 Comparison of the features extracted by trained neural networks with the manually determined features

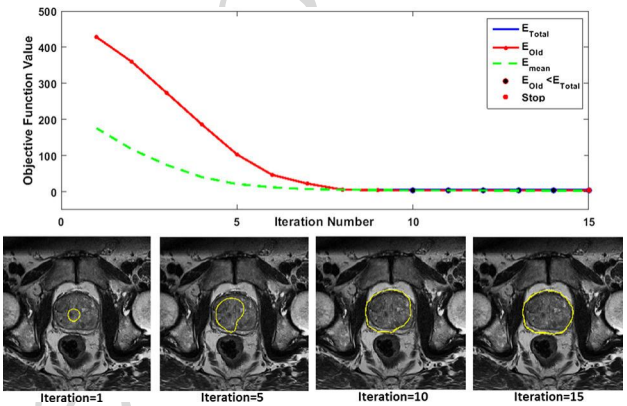

Fig. 7 The segmentation stage. Up: the effect of the searching algorithm on the objective function value. Below: the prostate area is extract using VFC active contour

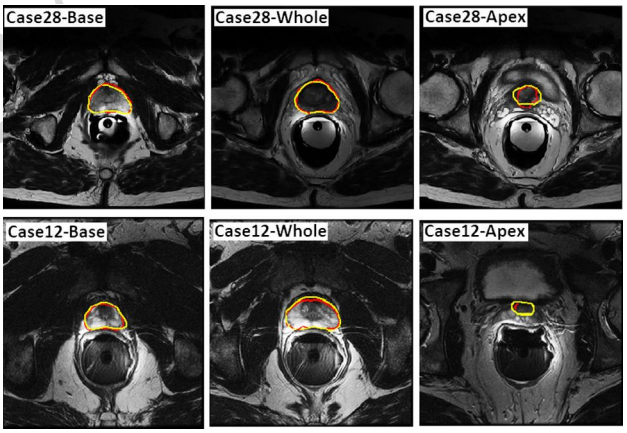

Fig. 8 Qualitative segmentation results of the prostate in testing data set. The yellow and red contours indicate the ground truth and our segmentation results. The shadows, artifacts and the tissue similarity decrease the segmentation accuracy in the Apex slices. The figures are available in the PROMISE12 challenge website

Journal: 11760 MS: 1320 TYPESET DISK LE CP Disp.:2018/6/16 Pages: 9 Layout: Large

Table 1 Evaluation of the presented method based on the DSC, H.D, ABD and RVD indexes

Metric	Whole	Base	Apex
DSC			
Average	0.89 ± 0.03	0.88 ± 0.04	0.8 ± 0.1
Score	85.89 ± 4.29	86.4 ± 4.75	85.11 ± 7.13
H.D			
Average	5.34 ± 1.38	5.31 ± 1.79	6.31 ± 2.27
Score	85.79 ± 3.69	87.31 ± 4.2	85.11 ± 5.37
ABD			
Average	1.86 ± 0.33	1.99 ± 0.53	2.57 ± 0.8
Score	84.6 ± 2.7	86.45 ± 3.58	84.85 ± 5.06
RVD			
Average	7.67 ± 7.91	12.96 ± 8.83	24.67 ± 25.9
Score	82 ± 18.67	84.9 ± 10.65	81.82 ± 18.8

Table 2 Quantitative comparison between the proposed method and other methods

Name	Rank	DSC (%)			H.D (mm)			ABD (mm)			RVD (%)			Score
		Whole	Base	Apex	Whole	Base	Apex	Whole	Base	Apex	Whole	Base	Apex	
CUMED [16]	3	**89.43**	86.42	**86.81**	5.54	5.41	**4.29**	1.95	2.13	**1.74**	**6.95**	**11.04**	**15.18**	86.65
			87.55 ± 4			**5.08 ± 1.58**			**1.94 ± 0.49**			**11.06 ± 11.39**		
Proposed Method	9	89.28	**87.55**	79.84	5.34	**5.32**	6.31	**1.86**	**2**	2.57	7.67	12.96	24.69	84.84
			86 ± 6			5.65 ± 1.81			2.14 ± 0.55			15.1 ± 14.21		
Imorphics [8]	11	87.99	86.06	84.53	5.94	5.45	4.73	2.1	2.18	1.96	11.65	13.33	20.75	84.36
			86.19 ± 6.97			5.07 ± 2.13			2.08 ± 0.88			15.24 ± 15.71		
Emory [10]	14	87.03	83.52	81.53	**5.04**	6.03	5.31	2.14	2.65	2.41	8.64	15.7	20.32	83.66
			84.03 ± 5.47			5.46 ± 1.31			2.4 ± 0.56			14.89 ± 9.88		
UdeM 2D [22]	16	87.42	84.93	84.16	6.12	6.44	4.71	2.17	2.39	2.07	12.37	18.37	21.9	83.02
			85.5 ± 5.6			5.76 ± 2.01			2.21 ± 0.65			17.55 ± 16.58		
CAMP TUM2 [18]	18	86.91	84.31	84.4	5.71	5.84	4.62	2.33	2.46	2.03	14.98	20.84	21.21	82.39
			85.21 ± 3.87			5.39 ± 1.5			2.27 ± 0.61			19.01 ± 17.1		
SIATMIDS [17]	22	84.29	83.2	75.75	6.17	6.21	6.09	2.49	2.58	2.76	12.6	16.16	27.51	80.85
			81.08 ± 3.33			6.15 ± 2.02			2.61 ± 0.81			18.76 ± 13.4		

where A is the region of interest that was segmented by the presented system and B is the region extracted manually. The relative volume difference was also calculated as follows:

$$\mathrm{RVD}(A, B) = 100 \times \left(\frac{A}{B} - 1\right) \tag{16}$$

The regular HD distance is described as follows:

$$\mathrm{HD}_m(X_s, Y_s) = \max_{x \in X_s}(\min_{y \in Y_s} d(x, y))$$
$$\mathrm{HD}(X_s, Y_s) = \max(\mathrm{HD}_m(X_s, Y_s), \mathrm{HD}_m(Y_s, X_s)) \tag{17}$$

where X_s and Y_s are the surface points set of the reference and algorithm segmentation, and d, is the Euclidean distance operand. Finally, the average boundary distance (ABD) is given by:

$$\mathrm{ABD}_{(X_s, Y_s)} = \frac{\left(\sum_{x \in X_s} \min_{y \in Y_s} d(x, y) + \sum_{y \in Y_s} \min_{x \in X_s} d(x, y)\right)}{X_s + Y_s} \tag{18}$$

Table 1 shows the results of our proposed system based on the mentioned indexes. The average of DSC, HD, ABD and RVD for all of the test images are 0.86 ± 0.06, 5.65 mm ± 1.81 mm, 2.57 mm ± 0.8 mm and 15.1 ± 14.21, respectively. According to the examinational results, the current work was ranked among the top 10 of the presented

Journal: 11760 MS: 1320 TYPESET DISK LE CP Disp.:2018/6/16 Pages: 9 Layout: Large

method. As shown in Table 2, the proposed method has a good performance as compared to the other works in the base and middle slices. In the mentioned slices, the averages of DSC, HD and ABD, for CUMED [16] are 89.43%, 5.54 and 1.95, in middle slices, and 86.42%, 5.41 and 2.13, in base slices. Similar indexes for the presented method are 89.28%, 5.34 and 1.86 in middle slices, and 87.55% 5.32 and 2, in base slices. However, based on the mentioned problems in Sect. 3, the segmentation accuracy was dropped in Apex slices.

5 Conclusion

In this paper, a new method for prostate segmentation in MR images was presented. This approach is a combination of VFC contours, MLP neural networks and several image processing techniques. According to the experimental results, the preprocessing stage can appropriately smooth images and reduce the disruptive effects of roughness and noise. Therefore, the disadvantages of GVF and the traditional active contour segmentation methods, which is their sensitivity to noise, have been eliminated. Additionally, preprocessing steps were utilized to prepare MR images for segmentation. During this stage, the image noise is reduced by applying a Sticks filter and morphology operators. This process also reduces the tolerance of the pixels intensity for the same regions in image. A novel and fast approach to automatically locate an initial point was introduced using MLP neural network, which improved the implementation time and accuracy of the algorithm. In the proposed algorithm, the VFC active contour is used to segment the prostate in the absence of strong edges that are removed by shadowing artifacts. This algorithm consumes less execution time when compared with the GVF. Furthermore, our implementation is an appropriate approach that quickly and accurately detects prostate regions in MR images as demonstrated in Sect. 3. The proposed algorithm on "Prostate MR Image Segmentation 2012 (PROMISE12)" challenge was evaluated, and the DCS accuracy of $86 \pm 6\%$ was obtained. Reducing the execution time, developing effective approaches to measure prostate volume, direct 3-D prostate segmentation in MR images and increasing the segmentation accuracy in Apex slices are subjects of interest for future research.

References

1. Cancer Facts and Figures. http://www.cancer.org (2017)
2. Siegel, R.L., Miller, K.D., Jemal, A.: Cancer statistics, 2016. CA Cancer J. Clin. **66**(1), 7–30 (2016). https://doi.org/10.3322/caac.21332
3. Ghose, S., Oliver, A., Marti, R., Llado, X., Vilanova, J.C., Freixenet, J., Mitra, J., Sidib, D., Meriaudeau, F.: A survey of prostate segmentation methodologies in ultrasound, magnetic resonance and computed tomography images. Computer Methods Programs Biomed. **108**(1), 262–287 (2012). https://doi.org/10.1016/j.cmpb.2012.04.006
4. Liu, X., Haider, M.A., Yetik, I.S.: Unsupervised 3D prostate segmentation based on diffusion-weighted imaging MRI using active contour models with a shape prior. J. Electr. Comput. Eng. **2011**, 11 (2011). https://doi.org/10.1155/2011/410912
5. Qiu, W., Yuan, J., Ukwatta, E., Tessier, D., Fenster, A.: Rotational-slice-based prostate segmentation using level set with shape constraint for 3D end-firing TRUS guided biopsy. Med. Image Comput. Comput. Assist. Interv. MICCAI **2012**, 537–544 (2012). https://doi.org/10.1007/978-3-642-33415-3_66
6. Qiu, W., Yuan, J., Ukwatta, E., Sun, Y., Rajchl, M., Fenster, A.: Fast globally optimal segmentation of 3d prostate MRI with axial symmetry prior. In: International Conference on Medical Image Computing and Computer-Assisted Intervention, pp. 198–205. Springer, Berlin (2013). https://doi.org/10.1118/1.4810968
7. Yan, P., Cheeseborough, J.C., Chao, K.C.: Automatic shape-based level set segmentation for needle tracking in 3-D TRUS-guided prostate brachytherapy. Ultrasound Med. Biol. **38**(9), 1626–1636 (2012). https://doi.org/10.1016/j.ulterasmedbio.2012.02.11
8. Vincent, G., Guillard, G., Bowes, M.: Fully automatic segmentation of the prostate using active appearance models. In: MICCAI Grand Challenge: Prostate MR Image Segmentation 2012 (2012)
9. Mahapatra, D.: Graph cut based automatic prostate segmentation using learned semantic information. In: 2013 IEEE 10th International Symposium on Biomedical Imaging (ISBI), pp. 1316–1319. IEEE (2013). https://doi.org/10.1109/ISBI.2013.6556774
10. Tian, Z., Liu, L., Zhang, Z., Fei, B.: Superpixel-based segmentation for 3D prostate MR images. IEEE Trans. Med. Imaging **35**(3), 791–801 (2016). https://doi.org/10.1109/TMI.2015.2496296
11. Egger, J., Bauer, M., Kuhnt, D., Carl, B., Kappus, C., Freisleben, B., Nimsky, C.: Nugget-cut: a segmentation scheme for spherically- and elliptically-shaped 3D objects. In: Pattern Recognition, pp. 373–382 (2010). https://doi.org/10.1007/978-3-642-15986-2_38
12. Gao, Y., Wang, L., Shao, Y., Shen, D.: Learning distance transform for boundary detection and deformable segmentation in CT prostate images. In: International Workshop on Machine Learning in Medical Imaging, pp. 93–100. Springer (2014). https://doi.org/10.1007/978-3-319-10581-9_12
13. Padgett, K., Swallen, A., Nelson, A., Pollack, A., Stoyanova, R.: SU-F-J-171: robust atlas based segmentation of the prostate and peripheral zone regions on MRI utilizing multiple MRI system vendors. Med. Phys. **43**(6Part11), 3447–3447 (2016). https://doi.org/10.1118/1.4956079
14. Khurd, P., Grady, L., Gajera, K., Diallo, M., Gall, P., Requardt, M., Kiefer, B., Weiss, C., Kamen, A.: Facilitating 3D spectroscopic imaging through automatic prostate localization in MR images using random Walker segmentation initialized via boosted classifiers. Prostate Cancer Imaging **6963**, 47–56 (2011). https://doi.org/10.1007/978-3-642-23944-1_5
15. Ghose, S., Mitra, J., Oliver, A., Marti, R., Llado, X., Freixenet, J., Vilanova, J.C., Comet, J., Sidib, D., Meriaudeau, F.: A supervised learning framework for automatic prostate segmentation in trans rectal ultrasound images. In: International Conference on Advanced Concepts for Intelligent Vision Systems, pp. 190–200. Springer (2012). https://doi.org/10.1007/978-3-642-33140-4_17
16. Yu, L., Yang, X., Chen, H., Qin, J., Heng, P.-A.: Volumetric convNets with mixed residual connections for automated prostate segmentation from 3D MR images. In: AAAI 2017, pp. 66–72 (2017)
17. He, B., Xiao, D., Hu, Q., Jia, F.: Automatic magnetic resonance image prostate segmentation based on adaptive feature learning

Journal: 11760 MS: 1320 TYPESET DISK LE CP Disp.:2018/6/16 Pages: 9 Layout: Large

probability boosting tree initialization and CNN-ASM refinement. IEEE Access (2017). https://doi.org/10.1109/ACCESS.2017.2781278
18. Milletari, F., Navab, N., Ahmadi, S.-A.: V-net: fully convolutional neural networks for volumetric medical image segmentation. In: 2016 Fourth International Conference on 3D Vision (3DV), pp. 565–571. IEEE (2016). https://doi.org/10.1109/3DV.2016.79
19. Xiong, W., Li, A.L., Ong, S.H., Sun, Y.: Automatic 3D prostate MR image segmentation using graph cuts and level sets with shape prior. In: Pacific-Rim Conference on Multimedia, pp. 211–220. Springer (2013). https://doi.org/10.1007/978-3-319-03731-8_20
20. Martin, S., Troccaz, J., Daanen, V.: Automated segmentation of the prostate in 3D MR images using a probabilistic atlas and a spatially constrained deformable model. Med. Phys. **37**(4), 1579–1590 (2010). https://doi.org/10.1118/1.3315367
21. Tsai, A., Yezzi, A., Wells, W., Tempany, C., Tucker, D., Fan, A., Grimson, W.E., Willsky, A.: A shape-based approach to the segmentation of medical imagery using level sets. IEEE Trans. Med. Imaging **22**(2), 137–154 (2003). https://doi.org/10.1109/TMI.2002.808355
22. Drozdzal, M., Chartrand, G., Vorontsov, E., Shakeri, M., Di Jorio, L., Tang, A., Romero, A., Bengio, Y., Pal, C., Kadoury, S.: Learning normalized inputs for iterative estimation in medical image segmentation. Med. Image Anal. **44**, 1–13 (2018). https://doi.org/10.1016/j.media.2017.11.005
23. Li, B., Acton, S.T.: Active contour external force using vector field convolution for image segmentation. IEEE Trans. Image Process. **16**(8), 2096–2106 (2007). https://doi.org/10.1109/TIP.2007.899601
24. Awad, J., Abdel-Galil, T., Salama, M., Tizhoosh, H., Fenster, A., Rizkalla, K., Downey, D.: Prostate's boundary detection in transrectal ultrasound images using scanning technique. In: Canadian Conference on Electrical and Computer Engineering, 2003. IEEE CCECE 2003, pp. 1199–1202. IEEE (2003). https://doi.org/10.1109/CCECE.2003.1226113
25. Demuth, H.B., Beale, M.H., De Jess, O., Hagan, M.T.: Neural Network Design, 2nd edn. Martin Hagan, USA (2014)
26. Yuan, D., Lu, S.: Simulated static electric field (SSEF) snake for deformable models. In: Proceedings of the 16th International Conference on Pattern Recognition, 2002, pp. 83–86. IEEE (2002). https://doi.org/10.1109/ICPR.2002.1044618
27. Matsumoto, T., Hanawa, T.: A fast algorithm for solving the Poisson equation on a nested grid. Astrophys. J. **583**(1), 296 (2003). https://doi.org/10.1086/345338

Journal: **11760** MS: **1320** ☐ TYPESET ☐ DISK ☐ LE ☐ CP Disp.:**2018/6/16** Pages: **9** Layout: **Large**